Identifying Radiation Belt Electron Source and Loss Processes by Assimilating Spacecraft Data in a Three-Dimensional Diffusion Model

S. Cervantes[1,2], Y. Y. Shprits[1,2,3], N. A. Aseev[1,2], A. Y. Drozdov[3], A. Castillo[1,2], and C. Stolle[1,4]

[1]Helmholtz Centre Potsdam, GFZ German Research Centre for Geosciences, Potsdam, Germany, [2]Institute of Physics and Astronomy, University of Potsdam, Potsdam, Germany, [3]Department of Earth, Planetary, and Space Sciences, University of California, Los Angeles, CA, USA, [4]Faculty of Science, University of Potsdam, Potsdam, Germany

Abstract Data assimilation aims to blend incomplete and inaccurate data with physics-based dynamical models. In the Earth's radiation belts, it is used to reconstruct electron phase space density, and it has become an increasingly important tool in validating our current understanding of radiation belt dynamics, identifying new physical processes, and predicting the near-Earth hazardous radiation environment. In this study, we perform reanalysis of the sparse measurements from four spacecraft using the three-dimensional Versatile Electron Radiation Belt diffusion model and a split-operator Kalman filter over a 6-month period from 1 October 2012 to 1 April 2013. In comparison to previous works, our 3-D model accounts for more physical processes, namely, mixed pitch angle-energy diffusion, scattering by Electromagnetic Ion Cyclotron waves, and magnetopause shadowing. We describe how data assimilation, by means of the innovation vector, can be used to account for missing physics in the model. We use this method to identify the radial distances from the Earth and the geomagnetic conditions where our model is inconsistent with the measured phase space density for different values of the invariants μ and K. As a result, the Kalman filter adjusts the predictions in order to match the observations, and we interpret this as evidence of where and when additional source or loss processes are active. The current work demonstrates that 3-D data assimilation provides a comprehensive picture of the radiation belt electrons and is a crucial step toward performing reanalysis using measurements from ongoing and future missions.

1. Introduction

The Earth's radiation belts consist of protons and electrons trapped by the Earth's magnetic field. The inner electron belt is usually located below 2 Earth radii (R_E) and is relatively stable. In contrast, the outer belt may extend from approximately 3 to 7 R_E, is very dynamic, can vary by several orders of magnitude over a few hours (Rothwell & McIlwain, 1960; Craven, 1966), and is correlated with geomagnetic activity. In addition, the outer belt consists of high-energy particles (from ∼100 keV to several tens of MeV), which pose a significant hazard to satellites in space (Baker et al., 1998, 2018; Baker, 2002; Green et al., 2017).

One of the space weather impacts to satellites is known as "deep-dielectric charging." Electrons with energies of ∼100 keV and up to multiple MeV can readily penetrate spacecraft shielding, bury themselves in dielectric materials deep within spacecraft subsystems, such as circuit boards or cable insulators, and accumulate on ungrounded metal. As charge builds up, this can lead to electrical breakdown in the vicinity of sensitive electronics (Fennell et al., 2001; Lohmeyer et al., 2015). Another kind of space weather impact is called "surface charging." Lower-energy electrons, from 10 to 100 keV, cannot penetrate the shielding but can accumulate on satellite surfaces. Charge buildup may lead to high voltages, damaging electrostatic discharges, and electromagnetic interference that can disorient the satellite. Mazur et al. (2011) presented the high-voltage increase in the LICA instrument on board the SAMPEX satellite as an example of a surface charging anomaly.

It is evident from the above description that a wide variety of impacts on spacecraft systems can be caused by the radiation belts. Therefore, knowledge of the outer belt dynamics is of particular importance since it spatially overlaps with many communication and scientific spacecraft orbits. Understanding the mechanisms responsible for the acceleration and loss of electrons is essential for predicting the response of the radiation belts to geomagnetic disturbances.

However, the analysis of spacecraft data poses a number of challenges. Satellite measurements are often limited to a restricted range of L shells, pitch angles, and energies, which complicates the data analysis geared toward reproducing the global state of the radiation belts. Additionally, the manual analysis of observations is a challenging task, while an automated analysis is complicated by the fact that measurements at different L shells are taken at different points along the spacecraft orbit and therefore at different times. Moreover, fluxes of energetic electrons in the outer belt change on timescales shorter than a typical satellite orbital period; thus, it is impossible to observe the instantaneous radial profiles of fluxes.

Similar challenges to those mentioned above were faced by the atmospheric sciences in the 1970s (Kalnay, 2003). A powerful method, inherited from the engineering of navigation systems and referred to as "data assimilation," was successfully applied to accomplish better weather predictions. This term denotes a process in which observations are merged together with a dynamical numerical model in order to determine the state of the atmosphere as accurately as possible (Talagrand, 1997). Data assimilation allows us to fill in the spatial and temporal gaps left by sparse measurements and to combine them with a physics-based model according to their underlying error structure, and the result is typically referred to as "reanalysis." Some of the most popular data assimilation methods are the standard Kalman filter (KF) (Kalman, 1960), the extended Kalman filter (Jazwinski, 1970), and the ensemble Kalman filter (Evensen, 1994).

Naehr and Toffoletto (2005) were among the first to show the potential of data assimilation to significantly improve the forecasting capabilities of radiation belt models. Kondrashov et al. (2007) used the extended Kalman filter and Combined Release and Radiation Effects Satellite (CRRES) observations to estimate the electron phase space density (PSD) and to infer unknown parameters in a model. Shprits et al. (2007) and Koller et al. (2007) performed data assimilation with a simple radial diffusion model and demonstrated how it can be used to identify and adjust for missing physics in the model.

Furthermore, Ni, Shprits, Nagai, et al. (2009) used four empirical external magnetic field models and found that combined reanalyses are relatively insensitive to the choice of magnetic field model. The results also showed that the errors of PSD obtained by assimilating multiple satellite measurements at different locations can be smaller than the errors of individual satellite reconstructions. Daae et al. (2011) tested the sensitivity of the reanalysis of radiation belt PSD to the assumed outer boundary conditions and loss model and demonstrated that the KF performs remarkably well when sufficient data is available at all considered L shells for the assimilation. More recently, Shprits et al. (2012) performed a long-term multispacecraft reanalysis and found a good correlation between the location of the peak of the PSD and the plasmapause location, and investigated the link between PSD dropouts and solar wind dynamic pressure increases.

Several recent studies have employed 3-D diffusion models accounting for radial, pitch angle, and energy diffusion (Bourdarie & Maget, 2012; Kellerman et al., 2014). Such 3-D models potentially account for more physical processes and use the knowledge of the dynamics of pitch angle distributions and energy spectra. Shprits, Kellerman, et al. (2013) suggested an operator splitting method that allowed to use the KF for 3-D diffusion codes and verified it on 2-month CRRES data.

The purpose of this study is to incorporate the following processes into the 3-D Versatile Electron Radiation Belt Code (VERB-3D) data assimilation scheme, absent in previous studies: mixed pitch angle-energy diffusion, scattering by electromagnetic ion cyclotron (EMIC) waves, and magnetopause shadowing. Their relevance to the radiation belt dynamics has been evaluated in earlier works, based either on observations or model simulations (Albert & Young, 2005; Albert et al., 2009; Drozdov et al., 2015, 2017; Shprits et al., 2006, 2008, 2016, 2017; Shprits, Subbotin, et al., 2013; Subbotin et al., 2010; Turner et al., 2012; Turner, Angelopoulos, Li, et al., 2014; Turner, Angelopoulos, Morley, et al., 2014; Usanova et al., 2014; Xiang et al., 2017; Xiao et al., 2010; Yu et al., 2013). However, their effect on the reanalysis has not yet been investigated and objectively quantified.

In the current work, we perform a combination of the VERB-3D code with data from the Van Allen Probes (formerly known as the Radiation Belt Storm Probes) and the Geostationary Operational Environmental Satellites (GOES) by means of a split-operator KF (Shprits, Kellerman, et al., 2013) from 1 October 2012 to 1 April 2013. We perform multiple reanalyses by systematically adding, one by one, the above-mentioned processes. The innovation vector, a measure on how the observations and the model predictions differ, is inspected for each reanalysis and for various values of the adiabatic invariants μ and K. We interpret this measure as an evidence of the effect of these mechanisms in the dynamics of the radiation belt electrons.

Furthermore, the radial distance from the Earth and the geomagnetic conditions under which each physical process operates are also identified by means of the innovation vector.

The outline of this paper is as follows: Our radiation belt model and the spacecraft databases used in this study are presented in sections 2 and 3, respectively, followed by a description of the standard KF as the overarching algorithm blending data and model predictions in section 4. Section 5 shows the 6-month reanalysis results of electron PSD, and section 6 presents how the Kalman innovation adds source and loss terms to the radiation belt model. The results are discussed and the main conclusions of the study are summarized in section 7. The definitions of adiabatic invariants are given in Appendix A.

2. VERB Code

2.1. Model Description

The VERB-3D code models the evolution of electron PSD by solving the modified 3-D Fokker-Planck diffusion equation that incorporates radial diffusion, energy diffusion, pitch angle scattering, and mixed diffusion into the drift- and bounce-averaged particle PSD (Schulz & Lanzerotti, 1974). Diffusion is produced by resonant wave-particle interactions with various waves in the magnetosphere. Radial diffusion is caused by ultralow frequency waves, while pitch angle, energy, and mixed diffusion are caused by whistler mode and EMIC waves.

The 3-D time-dependent Fokker-Planck equation for the PSD evolution of relativistic electrons can be written in terms of the L shell, equatorial pitch angle α_0, and relativistic momentum p, following Shprits et al. (2009) and Subbotin and Shprits (2009):

$$
\begin{aligned}
\frac{\partial f}{\partial t} =& L^{*2} \frac{\partial}{\partial L^*}\bigg|_{\mu,J} \left(\frac{1}{L^{*2}} D_{L^*L^*} \frac{\partial f}{\partial L^*}\bigg|_{\mu,J} \right) + \frac{1}{p^2} \frac{\partial f}{\partial p}\bigg|_{\alpha_0,L^*} p^2 \left(D_{pp} \frac{\partial f}{\partial p}\bigg|_{\alpha_0,L^*} + D_{\alpha_0 p} \frac{\partial f}{\partial \alpha_0}\bigg|_{p,L^*} \right) \\
&+ \frac{1}{T(\alpha_0)\sin(2\alpha_0)} \frac{\partial}{\partial \alpha_0}\bigg|_{p,L^*} T(\alpha_0)\sin(2\alpha_0) \left(D_{\alpha_0\alpha_0} \frac{\partial f}{\partial \alpha_0}\bigg|_{p,L^*} + D_{\alpha_0 p} \frac{\partial f}{\partial p}\bigg|_{\alpha_0,L^*} \right) - \frac{f}{\tau}
\end{aligned}
\tag{1}
$$

where f is the electron PSD, t is time, μ and J are the first and second adiabatic invariants (see Appendix A), respectively, and L^* is inversely related to the third adiabatic invariant Φ and is constant along the particle's drift path. $D_{L^*L^*}$, D_{pp}, $D_{\alpha_0\alpha_0}$, and $D_{\alpha_0 p}$ are the bounce-averaged radial, energy, pitch angle, and mixed pitch angle-energy diffusion coefficients, respectively. The lifetime parameter τ accounts for losses of particles inside the loss cone due to collisions with atmospheric neutrals, assumed to be infinite outside the loss cone and equal to a quarter of the electron bounce time inside the loss cone. $T(\alpha_0)$ is a function related to the bounce frequency (Schulz and Lanzerotti, 1974).

The parameterization of the radial diffusion coefficients due to magnetic fluctuations is adopted from Brautigam and Albert (2000). The bounce-averaged diffusion coefficients for hiss and dayside and nightside chorus waves are computed using the Full Diffusion Code (Shprits & Ni, 2009). The parameters for hiss are taken from Orlova et al. (2014), while for dayside and nightside chorus the parameterization of Orlova and Shprits (2014) is used. The spectral properties from Meredith et al. (2014) are used to calculate diffusion coefficients for helium band EMIC waves. In accordance with Drozdov et al. (2017), EMIC waves are included in the simulation when the solar wind dynamic pressure is greater than or equal to 3 nPa. The location of the plasmapause is calculated following Carpenter and Anderson (1992) as

$$
L_{pp} = 5.6 - 0.46\,Kp_{\max 24},
\tag{2}
$$

where $Kp_{\max 24}$ is the maximum Kp value in the preceding 24 hr.

The 3-D VERB code includes the Last Closed Drift Shell (LCDS) as a function of time and invariant K. The LCDS is introduced to include physics associated with magnetopause shadowing. In this study, the Tsyganenko and Sitnov (2007) model is used to determine the LCDS. Since the magnetopause shadowing effect is dependent on the drift period, we use an energy-dependent loss mechanism, as suggested by Drozdov et al. (2015). Losses due to magnetopause shadowing are simulated with an exponential decay of the electron PSD outside the LCDS location, as follows:

$$
f(t, L^* > \mathrm{LCDS}(t)) = f(t)e^{(-1/\tau_d)}.
\tag{3}
$$

Here, τ_d is the electron drift period calculated as (Walt, 2005):

$$\tau_d(s) = C_d \left(\frac{R_E}{R_0} \right) \frac{1}{\gamma \beta^2} \left[1 - 0.333 \left(\sin \alpha_0 \right)^{0.62} \right] \tag{4}$$

where $C_d = 1.557 \times 10^4$ for electrons, $\beta = \frac{v}{c}$, $\gamma = (1 - \beta^2)^{-1/2}$, $R_E = 6.37 \times 10^3$ km, and R_0 is the distance from the center of the Earth to the equatorial crossing point of a magnetic field line. As R_0 increases, the drift period decreases. In addition, as the electron energy increases, the drift period decreases.

2.2. Model Grid and Boundary Conditions

The computational grid has 29×101×91 points along radial, energy, and pitch angle dimension, respectively. Radial grid points are uniformly distributed, while energy and pitch angle grid points are logarithmically distributed. The L^* grid extends from 1 to 6.6 R_E. The energy grid is defined by a minimum of 0.01 MeV and a maximum of 10 MeV at the outer radial boundary $L^* = 6.6$. The pitch angle grid is set from 0.3° to 89.7°.

For the initial PSD we use the steady state solution of the radial diffusion equation. The solution of equation (1) requires six boundary conditions, two for each variable in the equation. In order to simulate the loss of electrons to the atmosphere, a lower radial boundary condition ($L^* = 1$) of $f = 0$ is used. The PSD required for the upper radial boundary condition ($L^* = 6.6$) is time-dependent and is obtained from the GOES observations. The lower pitch angle boundary condition is set to 0 to simulate precipitation loss of electrons into the loss cone in a weak diffusion regime. For the upper pitch angle boundary condition, a zero gradient is chosen to account for the flat pitch angle distribution observed at 90° (Horne et al., 2003). The upper energy boundary at 10 MeV is set to 0, while for the lower energy boundary, the PSD is set constant in time to represent a balance of convective source and loss processes.

3. Satellite Observations

In this study, in situ observations from four spacecraft are used in combination with the VERB-3D code: Van Allen Probes A and B, and GOES satellites 13 and 15. The observations cover a 6-month period from 1 October 2012 to 1 April 2013. In order to assimilate the data, they are converted from flux to PSD in phase space coordinates (L^*, μ, K). To do so, magnetic field information is required. The in situ magnetic field measurements are used to calculate μ, while to calculate K and L^* the Tsyganenko and Sitnov (2007) model is employed. Similar to Kellerman et al. (2014), the intercalibration of the observations from different satellites is performed using a PSD matching algorithm.

3.1. Van Allen Probes

The Van Allen Probes (Mauk et al., 2012; Stratton et al., 2012) were launched on 30 August 2012 to study the dynamical evolution of the radiation belts. Both spacecraft are equipped with identical suites of instruments designed for monitoring radiation belt particles and wave environment. The Radiation Belt Storm Probes-Energetic particle, Composition, and Thermal plasma suite measures particles with energies ranging from hot to ultrarelativistic (Spence et al., 2013), and it includes the Magnetic Electron Ion Spectrometer (Blake et al., 2013), and Relativistic Electron Proton Telescope (Baker et al., 2012) instruments.

3.2. GOES

The multimission GOES (Onsager et al., 1996; Singer et al., 1996) program is aimed at monitoring the near-Earth space, including operational meteorology and space weather. Data from the GOES 13 and 15 units, launched on 24 May 2006 and 4 March 2010, respectively, are used in this study. The GOES Space Environment Monitor subsystem contains multiple instruments including the Energetic Particle Sensor/High Energy Proton and Alpha Detector instrument that measures the flux of protons, alpha particles, and electrons over an extensive range of energies. In particular, we employ data from the MAGnetospheric Electron Detector (Hanser, 2011) and Energetic Proton, Electron, and Alpha Detector (Hanser, 2011; Onsager et al., 1996) instruments.

4. Data Assimilation Using the Kalman Filter

Data assimilation is an algorithm that allows for an optimal combination of model results and sparse data from various sources, contaminated by noise and systematic errors (Kalman, 1960). The purpose of data assimilation is to find the most likely estimate of the unknown true state of a dynamic system using the information provided by the physical model and the available observations, considering both their uncertainties

and limitations. One popular technique for data assimilation is the Kalman filter (Kalman, 1960), an optimal recursive algorithm, which has found many applications such as the navigational system on the Apollo mission and Global Positioning System devices, operational weather forecasting, and ocean modeling (Kalnay, 2003; Lahoz et al., 2010; Sorenson, 1985). The methodology of the KF is outlined below.

4.1. Kalman Filter Methodology

For a given dynamic system described by a set of partial differential equations, the numerical algorithm can be presented in the following discrete form:

$$\mathbf{x}_k^f = \mathbf{M}_{k-1}\mathbf{x}_{k-1}^a \tag{5}$$

where the state vector $\mathbf{x}$ is composed of all model variables, which for our radiation belt model is the PSD on the numerical grid locations. $\mathbf{M}$ is a matrix of the numerical model, in our case, the discretized Fokker-Plank equation, and it advances the state vector $\mathbf{x}$ in discrete time intervals Δt. Superscripts f and a refer to forecast and analysis, respectively, and the subscript k shows the time step. The $\mathbf{x}_k^a$ is the best estimate of the state vector at time k, relying on the model and the available observations. The evolution of $\mathbf{x}_k^t$, where the superscript t refers to true, is assumed to be given by

$$\mathbf{x}_k^t = \mathbf{M}_{k-1}\mathbf{x}_{k-1}^t + \epsilon_k^m \tag{6}$$

where ϵ_k^m is the model error, represented by a spatially correlated ($\mathrm{E}(\epsilon^m \epsilon^{mT}) = \mathbf{Q}$) white noise ($\mathrm{E}(\epsilon^m) = 0$). The symbol E represents the expectation operator over time, and $\mathbf{Q}$ is the model covariance matrix.

The observations $\mathbf{y}_k^o$, where the superscript o refers to observed, are also assumed to be contaminated by errors:

$$\mathbf{y}_k^o = \mathbf{H}_k\mathbf{x}_k^t + \epsilon_k^o \tag{7}$$

where ϵ_k^o is the observational error, represented by a spatially correlated ($\mathrm{E}(\epsilon^o \epsilon^{oT}) = \mathbf{R}$) white noise ($\mathrm{E}(\epsilon^o) = 0$). $\mathbf{R}$ is the observational error covariance matrix. The observation matrix $\mathbf{H}_k$ maps the true space onto the observed space, and it accounts for the fact that usually the dimension of $\mathbf{y}_k^o$ is less than the dimension of $\mathbf{x}_k^t$ (i.e., only certain variables are observed).

During the update times, the forecast state vector is corrected by the data-driven innovation vector to yield the analysis state vector:

$$\mathbf{x}_k^a = \mathbf{x}_k^f + \mathbf{x}_k^i \tag{8}$$

where $\mathbf{x}_k^i = \mathbf{K}_k \left(\mathbf{y}_k^o - \mathbf{H}_k\mathbf{x}_k^f \right)$ is the innovation vector. $\mathbf{K}_k$ is the Kalman gain matrix calculated at each time step from a time-evolving forecast-error covariance matrix given by

$$\mathbf{P}_k^f = \mathbf{M}_{k-1}\mathbf{P}_{k-1}^a\mathbf{M}_{k-1}^T + \mathbf{Q}_{k-1} \tag{9}$$

On the analysis step the error covariance matrix is also updated:

$$\mathbf{P}_k^a = \left(\mathbf{I} - \mathbf{K}_k\mathbf{H}_k \right) \mathbf{P}_k^f \tag{10}$$

When no observations are available at time $k\Delta t$, $\mathbf{H}_k = 0$, only the forecast step is performed, $\mathbf{x}_k^a = \mathbf{x}_k^f$ and $\mathbf{P}_k^a = \mathbf{P}_k^f$. The Kalman gain matrix $\mathbf{K}_k$ in equation (7) is computed by minimizing the analysis error covariance $tr\mathbf{P}_k^a$, and it represents the optimal weights given to the observations when updating the model state vector:

$$\mathbf{K}_k = \mathbf{P}_k^f\mathbf{H}_k^T\left(\mathbf{H}_k\mathbf{P}_k^f\mathbf{H}_k^T + \mathbf{R}_k\right)^{-1} \tag{11}$$

The innovation vector $\mathbf{x}_k^i$ measures how much the new and additional information provided by the data modifies the model forecast to produce an optimal estimate of the state vector. The sign and the value of the innovation vector are determined by how much the observed and modeled values differ from each other, as well as by the estimated forecast and observational errors. If a model were perfect, it would predict exactly the incoming observations, and the innovation would be 0. From equation (11) we see that as the observational error covariance matrix $\mathbf{R}_k$ approaches 0, the Kalman gain $\mathbf{K}_k$ weights the innovation more heavily. On the
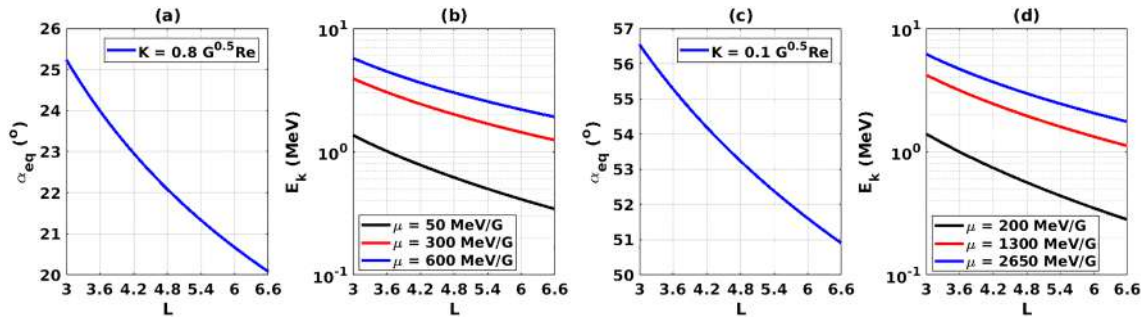
Figure 1. Dependence of equatorial pitch angle α_0 (a and c) and electron kinetic energy E_k (b and d) on L shell in a dipolar magnetic field, for the six pairs of (μ, K) investigated in the present study.

contrary, as the forecast error covariance matrix $\mathbf{P}_k^f$ approaches 0, the gain $\mathbf{K}_k$ weights the innovation less heavily. Ghil and Malanotte-Rizzoli (1991) present a detailed description of the KF algorithm.

The standard formulation of the KF assumes that the model and observational error covariance matrices are known. This rarely happens in practice and simple approximations are usually made. In the current study, the initial error covariance matrices are set equal to 0. The model error covariance matrix $\mathbf{Q}_k$ is a diagonal matrix with elements calculated as $q = Xf^2$, where $X = 0.5$ is the error and f is the PSD at the time of the assimilation. A similar form is assigned to the observational error covariance matrix $\mathbf{R}_k$. We use VERB-3D with a 1-hr time step, and the assimilation is performed at the same cadence using Van Allen Probes A and B and GOES 13 and 15 observations.

5. Combined Reanalysis of Electron PSD

In this section, we present radial profiles of PSD for a 6-month interval starting on 1 October 2012, on the basis of the methodology described in section 4. We focus on the evolution of PSD for two sets of three pairs of the adiabatic invariants μ and K, yielding six pairs in total. For the first set, the invariant K is equal to 0.8 $G^{0.5}$ R_E, with the following three different values of μ: 50, 300, and 600 MeV G^{-1}. For the second set, the invariant K equals 0.1 $G^{0.5}$ R_E, with the following three different values of μ: 200, 1300, and 2650 MeV G^{-1}. Their related equatorial pitch angle α_0 and electron kinetic energy E_k dependencies on the L shell for a dipole magnetic field are plotted in Figure 1, using the definitions given in Appendix A. The pitch angle of the electrons changes only by a few degrees, whereas electrons can lose (gain) a large amount of kinetic energy by radially diffusing outward (inward) by a few L shells.

At the heart of the outer radiation belt, namely, $L = 4.5$, for the chosen values of $K = 0.8$ $G^{0.5}$ R_E and $K = 0.1$ $G^{0.5}$ R_E, the equatorial pitch angles are approximately 22° and 52°, respectively. At $L = 4.5$ for the pairs ($\mu = 50$ MeV G^{-1}, $K = 0.8$ $G^{0.5}$ R_E) and ($\mu = 200$ MeV G^{-1}, $K = 0.1$ $G^{0.5}$ R_E), electron energies are ~0.7 MeV. For the pairs ($\mu = 300$ MeV G^{-1}, $K = 0.8$ $G^{0.5}$ R_E) and ($\mu = 1300$ MeV G^{-1}, $K = 0.1$ $G^{0.5}$ R_E), E_k is ~2.2 MeV, while for the pairs ($\mu = 600$ MeV G^{-1}, $K = 0.8$ $G^{0.5}$ R_E) and ($\mu = 2650$ MeV G^{-1}, $K = 0.1$ $G^{0.5}$ R_E), electron energies are ~ 3.3 MeV, at $L = 4.5$. Such a selection of pairs of adiabatic invariants allows us to compare three different populations of electrons at low and high equatorial pitch angles, with approximately the same energy variation across the outer radiation belt.

In total, we perform four data assimilation runs. The first one only accounts for radial diffusion due to ultralow frequency waves, and for pitch angle and energy diffusion due to chorus and hiss waves (hereinafter, 3-D diffusion), neglecting mixed diffusion, EMIC wave scattering, and losses due to magnetopause shadowing. In the other three runs, we systematically add one process at a time with respect to the previous run. For the second reanalysis we incorporate mixed pitch angle-energy diffusion, for the third one, scattering by EMIC waves, and for the last one, magnetopause shadowing.

The combined reanalyses based on the VERB-3D code and four satellite measurements, and accounting for 3-D diffusion, mixed pitch angle-energy diffusion, EMIC wave scattering, and magnetopause shadowing, are shown in Figures 2 and 3. From top to bottom, we present the 1-hr-averaged electron PSD versus L^* distribution for the four satellites and the assimilated radial profile of PSD at the above-mentioned pairs of
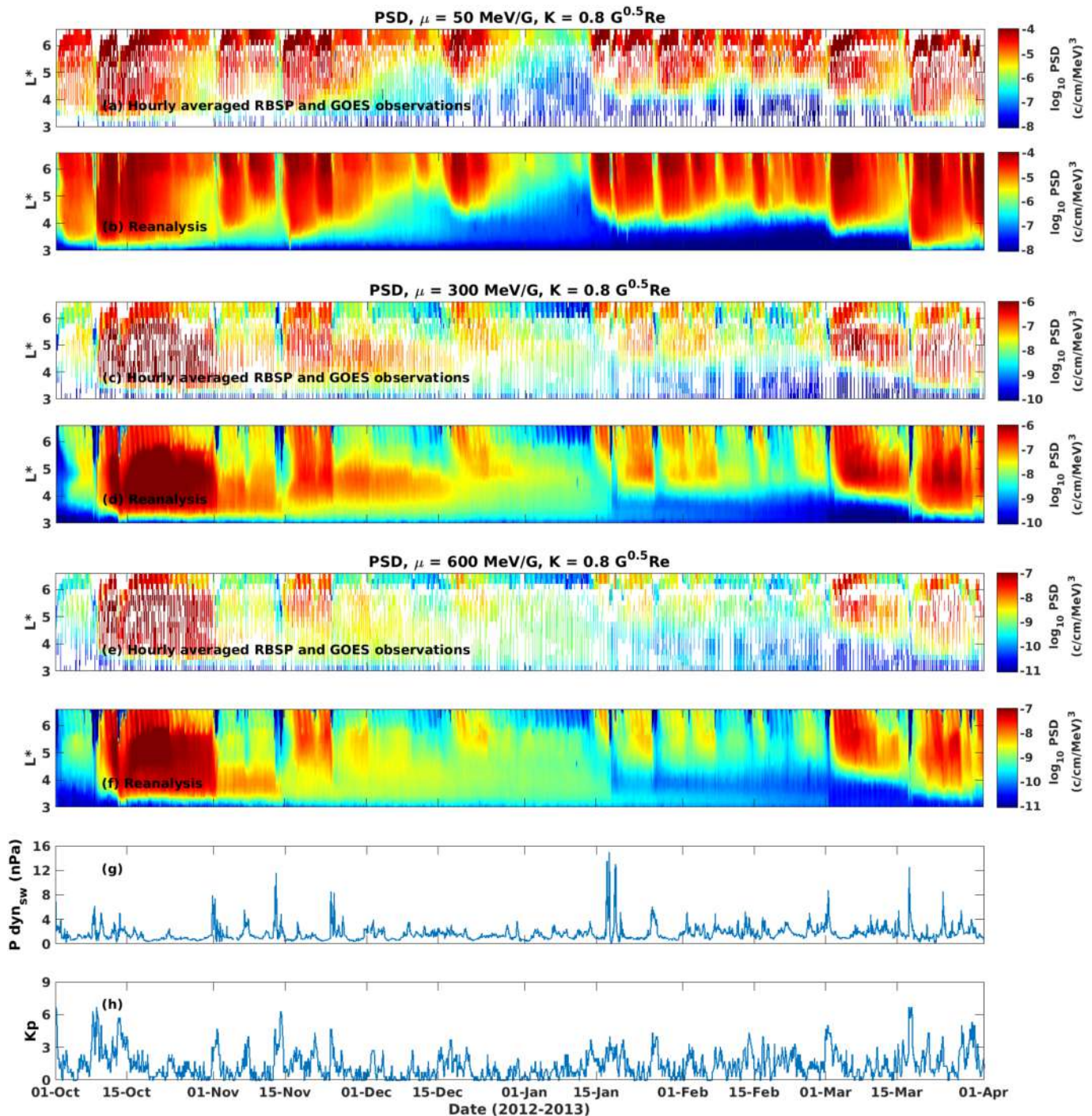
Figure 2. Evolution of electron PSD as a function of L^* and time from 1 October 2012 to 1 April 2013: (a) Van Allen Probes and GOES data, and (b) assimilated radial profile of PSD for $\mu = 50$ MeV G^{-1} and $K = 0.8$ $G^{0.5}$ R_E; (c and d) same as (a) and (b) but for $\mu = 300$ MeV G^{-1} and $K = 0.8$ $G^{0.5}$ R_E; (e and f) same as (a) and (b) but for $\mu = 600$ MeV G^{-1} and $K = 0.8$ $G^{0.5}$ R_E; (g) evolution of solar wind dynamic pressure, and (h) geomagnetic activity Kp index. The assimilative results of the combined reanalysis of electron PSD in this figure account for 3-D diffusion, mixed pitch angle-energy diffusion, scattering by EMIC waves, and magnetopause shadowing.
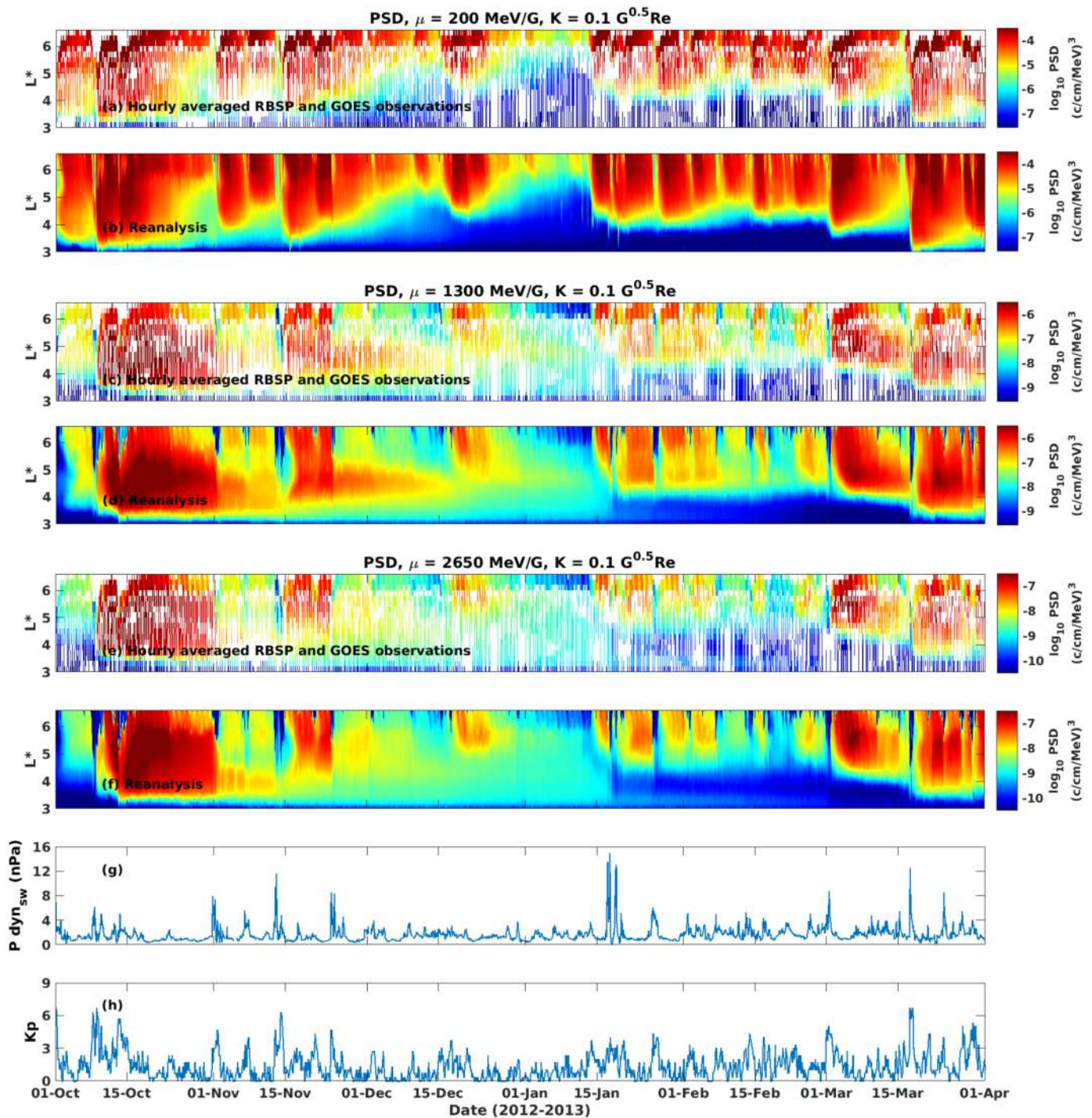
Figure 3. Same as Figure 2, but for the pairs of invariants $\mu = 200$ MeV G^{-1} and $K = 0.1$ G$^{0.5}$ R$_E$ (a and b); $\mu = 1300$ MeV G^{-1} and $K = 0.1$ G$^{0.5}$ R$_E$ (c and d); and $\mu = 2650$ MeV G^{-1} and $K = 0.1$ G$^{0.5}$ R$_E$ (e and f).

(μ, K). The last two panels show the solar wind dynamic pressure and the geomagnetic index Kp, respectively, obtained from the online OMNIWEB database with 1-hr resolution. As illustrated by the Kp index, there are several geomagnetic storms occurring during the six-month period of our study, the strongest ones reaching $Kp = 7-$ on 8 October 2012 and 17 March 2013. The Van Allen Probes measurements provide the electron PSD below $L^* = 5.8$, and the GOES measurements above $L^* \sim 6$, establishing a good radial coverage of observed PSD. Although the data clearly show a number of electron dropouts and enhancements, the
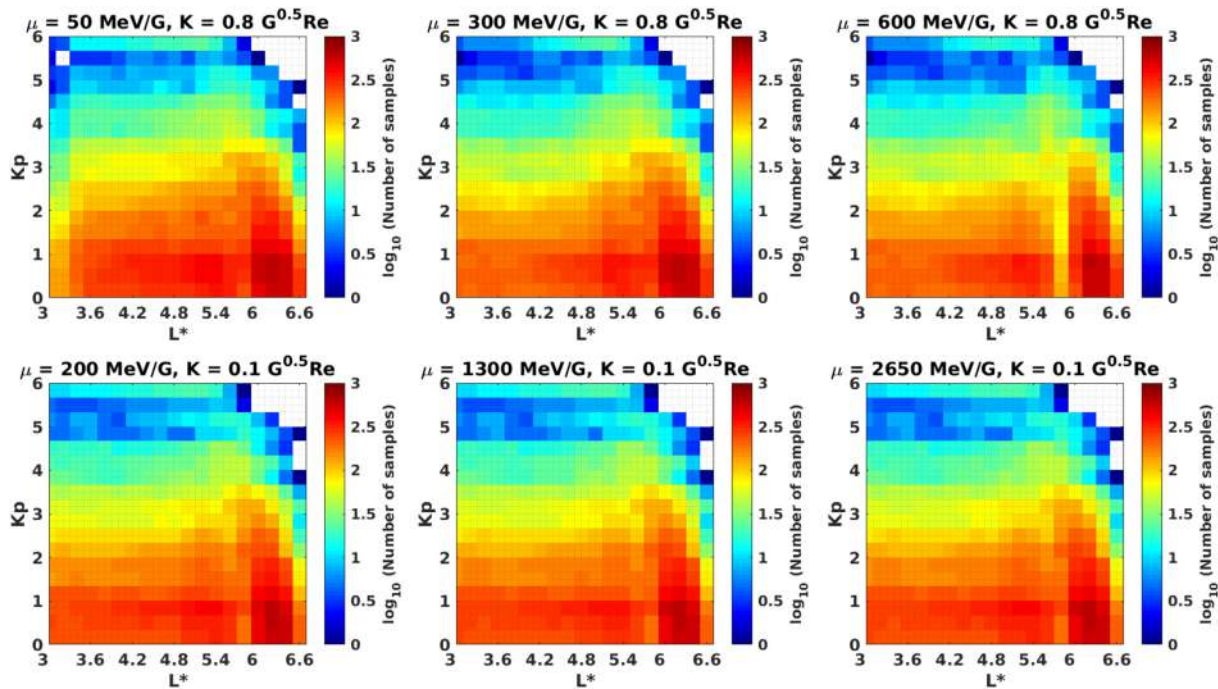
Figure 4. Distribution of the number of samples employed in the reanalyses of PSD binned in L^* and Kp for the indicated pairs of adiabatic invariants μ and K.

distribution is still sparse in space and time. After blending the observations with the VERB-3D code, the gaps are filled, as illustrated in panels (b), (d), and (f).

The temporal evolution of the assimilated PSD is strongly correlated with the geomagnetic activity as shown in Figures 2 and 3. In accordance with previous reanalysis studies (Ni, Shprits, Nagai, et al., 2009; Ni, Shprits, Thorne, et al., 2009; Ni et al., 2013; Shprits et al., 2012), sudden and substantial dropouts in PSD are observed during the main phase of geomagnetic storms, depleting electron PSD even down to $L^* = 4.6$, as on 17 March 2013, and lasting a few hours. These decreases occur right after sudden pulses of solar wind dynamic pressure, which are in turn associated with clear and pronounced compressions of the magnetopause. For example, on 17 January 2013 the solar wind dynamic pressure increased up to 14.8 nPa, and the LCDS moved inward down to $L^* = 5.2$, well below the geosynchronous orbit. On the other hand, most of the PSD peaks are seen during the recovery phase of the storms. Such buildups of PSD are gradual and in general extend from 4 to 5 R_E.

In addition, the dependence on energy of our magnetopause shadowing loss mechanism is evident when comparing panels (b), (d), and (f) of Figures 2 and 3. The loss effect is more pronounced at higher values of the invariant μ (lowermost reanalyses, panel f), where electron PSD is depleted faster than for lower values of μ (uppermost reanalyses, panel b).

6. Analysis of the Innovation Vector

As mentioned in section 4, the innovation vector adds or subtracts PSD from the predicted values, and it can be regarded as an indicator of the missing electron loss and source processes in the model. Shprits et al. (2007), Koller et al. (2007), and Daae et al. (2011) used it as a tool to understand the physical mechanisms responsible for the acceleration of electrons and interpreted its peaks as evidence of local acceleration, absent in the 1-D model employed in their studies.

To objectively investigate the effect of introducing several processes in our model, we calculated the hourly innovation vector for each L^*, binned it according to the Kp index, and computed the average innovation vector as a function of L^* and Kp for each of our four 6-month reanalyses and each of our six pairs of adiabatic invariants. The distribution of the number of measurements that were used for the reanalyses in terms of Kp is shown in Figure 4. Owing to the highly skewed distribution of samples toward low values of Kp, and the lack of measurements at high Kp and L^*, we restricted our analysis of the innovation vector to the intervals
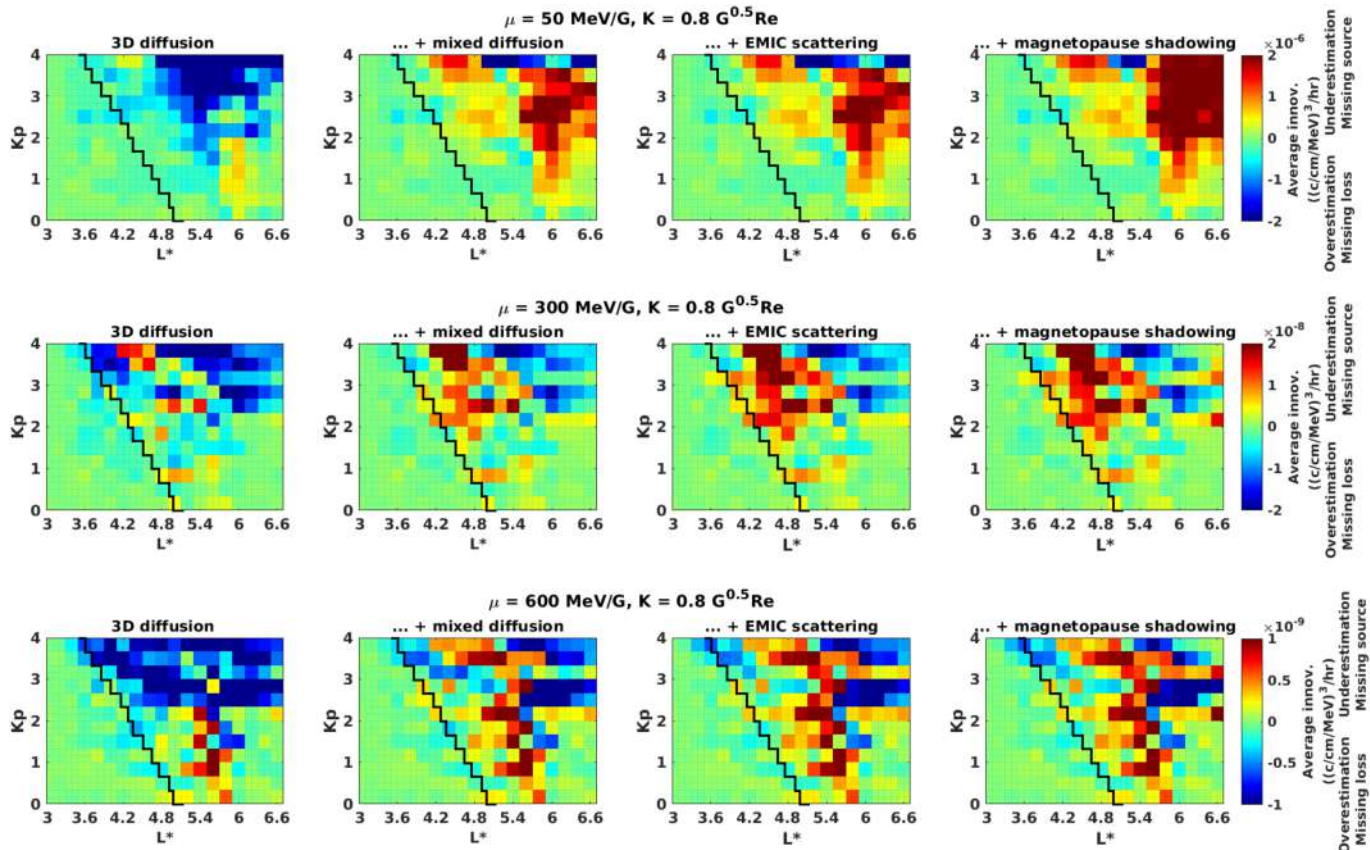
Figure 5. Innovation vector averaged over the interval October 2012 to March 2013 as function of L^* and Kp for electron PSD for the following pairs of invariants: $\mu = 50$ MeV G^{-1} and $K = 0.8$ G$^{0.5}$ R$_E$ (first row), $\mu = 300$ MeV G^{-1} and $K = 0.8$ G$^{0.5}$ R$_E$ (second row), and $\mu = 600$ MeV G^{-1} and $K = 0.8$ G$^{0.5}$ R$_E$ (third row). The first column corresponds to radial, pitch angle and energy diffusion (3-D) reanalysis, the second to reanalysis with the addition of mixed pitch angle-energy diffusion, the third to reanalysis including scattering by EMIC waves, and the last to reanalysis adding magnetopause shadowing. The solid black line indicates the estimated average location of the plasmapause, computed following Carpenter and Anderson (1992).

with $Kp < 4$. Evaluation of the innovation including intervals of high geomagnetic activity will be the subject of future research.

The average innovation vector as a function of L^* and Kp is shown in Figures 5 and 6, for the pairs of invariants with $K = 0.8$ G$^{0.5}$ R$_E$ and $K = 0.1$ G$^{0.5}$ R$_E$, respectively. Positive (negative) values denote an additional source (loss) term missing from the radiation belt model, and thus the KF adds (subtracts) PSD in order to compensate and to match the observations. In other words, the innovation is positive (negative) when the observations are significantly higher (lower) than the forecast, hence our model underestimates (overestimates) the electron PSD.

6.1. Average Innovation for PSD at $K = 0.8$ G$^{0.5}$ R$_E$ and Different Values of the Invariant μ

For the electrons with $\mu = 50$ MeV G^{-1} (Figure 5, first row), the average innovation using our model with 3-D diffusion shows enhanced overestimation of PSD extending from $L^* = 4.4$ to $L^* = 6.6$ for $Kp > 2$, and for $Kp < 2$ between $L^* = 5$ and $L^* = 5.6$. The addition of mixed pitch angle-energy diffusion significantly reduces this overestimation, and furthermore, it emphasizes a region of underestimation of PSD at large radial distances, extending from $L^* = 5.6$ to the outer boundary. The inclusion of EMIC waves does not change the average innovation vector, as the lower energy electrons (≤ 1 MeV) are in general unaffected by them (Horne & Thorne, 1998; Meredith et al., 2003). Lastly, incorporating magnetopause shadowing driven by the LCDS accentuates a region of large innovation at $L^* > 5.8$ for $Kp > 2$. This is indicative of a missing source in our radiation belt model, namely, earthward magnetospheric convection of electrons with keV energies from the tail region to the plasma sheet.

The average innovation vector of the 3-D reanalysis of the electrons with $\mu = 300$ MeV G^{-1} (Figure 5, second row) exhibits a region of large overestimation of PSD at all L^* for $Kp > 2+$. Such missing loss is then
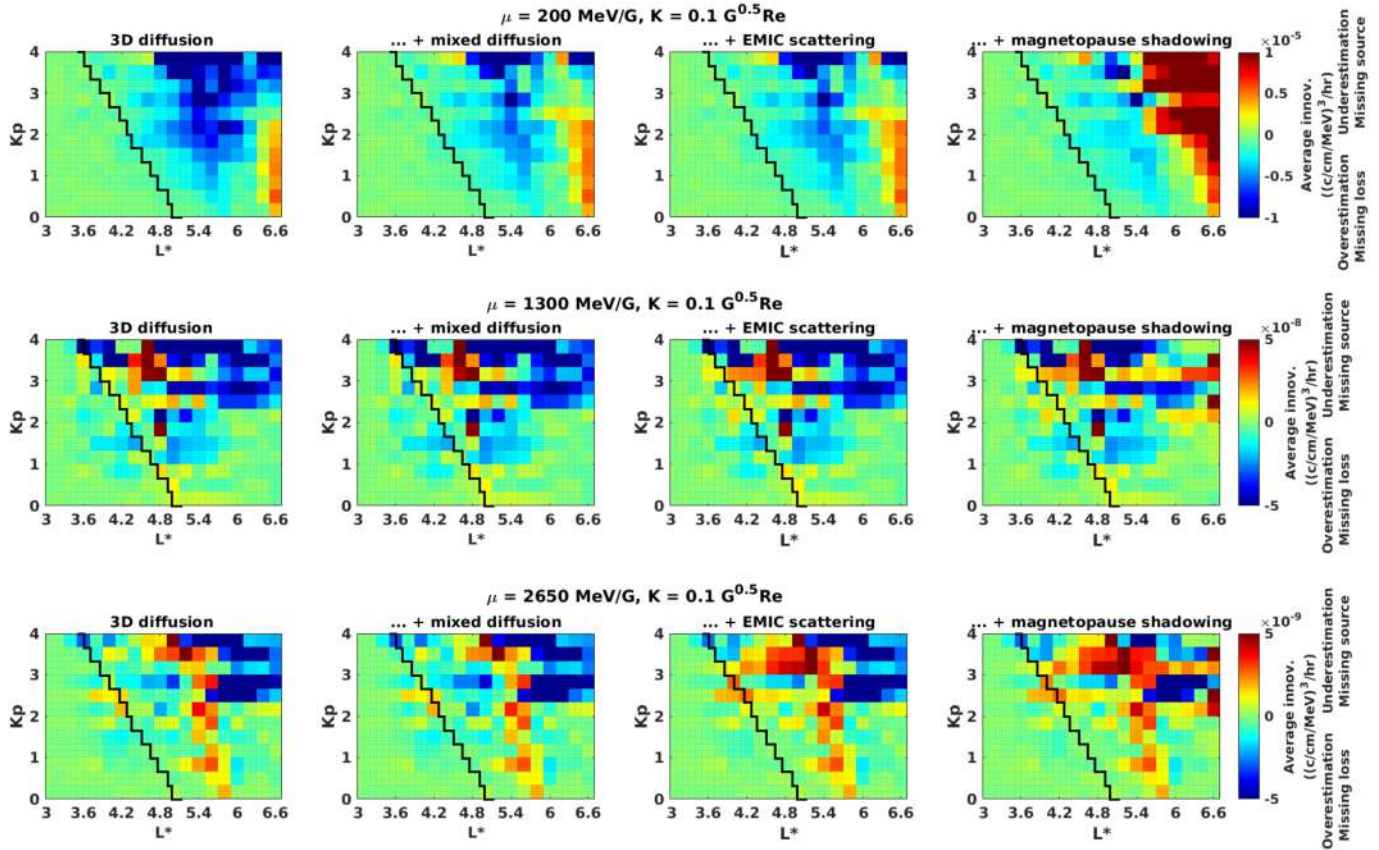
Figure 6. Same as Figure 6, for the pairs of invariants $\mu = 200$ MeV G^{-1} and $K = 0.1$ G$^{0.5}$ R$_E$ (first row), $\mu = 1300$ MeV G^{-1} and $K = 0.1$ G$^{0.5}$ R$_E$ (second row), and $\mu = 2650$ MeV G^{-1} and $K = 0.1$ G$^{0.5}$ R$_E$ (third row).

added when mixed pitch angle-energy diffusion is incorporated into our scheme, in particular at $L^* < 5.8$. Furthermore, scattering by EMIC waves effectively brings loss into our model, as the average innovation vector decreases for $L^* < 5.6$ and $Kp > 3$, which for this population of electrons corresponds to energies greater than 1.9 MeV. Note that the effect of EMIC waves is only observed close to the plasmapause and is negligible below 1.9 MeV. The innovation, when magnetopause shadowing and outward diffusion induced by it are included, acts as a loss process, especially for $Kp > 3$ and $L^* > 5.6$.

Finally, for the electrons with first invariant $\mu = 600$ MeV G^{-1} (Figure 5, third row), the PSD is largely overestimated when relying only on our 3-D model, hence the KF substracts PSD, particularly in the region extending from $Kp = 2$ to $Kp = 4$ at all L^*. The addition of both mixed pitch angle-energy diffusion and EMIC wave scattering acts as a loss process, mostly for $Kp > 2$ and $L^* < 5.8$, where the energy of electrons is larger than 2.2 MeV. Moreover, taking into account magnetopause shadowing reduces to some extent the overestimation of electron PSD at $L^* > 5.6$ and $Kp > 3$.

6.2. Average Innovation for PSD at $K = 0.1$ G$^{0.5}$ R$_E$ and Different Values of the Invariant μ

For the 3-D reanalysis of the electrons with $\mu = 200$ MeV G^{-1} (Figure 6, first row), the average innovation vector shows how our model accounting only for 3-D diffusion significantly overestimates PSD. As a result, the KF subtracts PSD between $L^* = 4.6$ and $L^* = 6.6$ for $Kp > 2+$, and from $L^* = 4.8$ to $L^* = 6.2$ for quieter geomagnetic conditions. Such a missing loss process is added when mixed pitch angle-energy diffusion is incorporated into our framework, particularly for $L^* < 6$. Due to the low energy of this population of electrons, the inclusion of EMIC wave scattering does not modify the average innovation vector. Moreover, considering magnetopause shadowing shows that a missing source process (magnetospheric convection) is operating between $L^* = 5.6$ and $L^* = 6.6$, similarly to the case with $\mu = 50$ MeV G^{-1} and $K = 0.8$ G$^{0.5}$ R$_E$.

The average innovation of the electrons with $\mu = 1,300$ MeV G^{-1} (Figure 6, second row) shows that for $L^* > 5$ and all geomagnetic conditions, PSD is overestimated by the 3-D model. However, introducing mixed

pitch angle-energy diffusion does not significantly affect this population. The addition of scattering by EMIC waves corrects for the PSD overestimation in the region between $Kp = 3$ and $Kp = 4$ for $L^* < 4.4$, where the energy of the electrons is greater than 2.3 MeV. Considering magnetopause shadowing brings further losses into our model, in particular for $Kp > 2$ and $L^* > 5.4$.

Lastly, the innovation of the 3-D reanalysis of the electrons with $\mu = 2650$ MeV G^{-1} (Figure 6, third row) shows, on average, a region of overestimation at $L^* > 5.8$ for $Kp > 2$, and for $Kp > 3-$ at $L^* < 5.2$. For this population, mixed pitch angle-energy diffusion does not introduce losses as was the case for the electrons with $K = 0.8$ G$^{0.5}$ R$_E$. In contrast, EMIC wave scattering effectively decreases PSD for $Kp > 2+$ and $L^* < 5.6$, where electrons have energies larger than 2.3 MeV, and magnetopause shadowing partially removes PSD at $L^* > 5.4$ and $Kp > 2+$.

7. Discussion and Conclusions

In this study, we show how data assimilation by means of a standard KF allows us to fill in the spatial and temporal gaps left by sparse in situ measurements, combine them with our radiation belt model, and as result, reconstruct electron PSD. In comparison to previous works, our model potentially accounts for more physical loss processes, and in the future, will allow us to further understand the dynamical evolution of radial profiles of PSD. Data assimilation can also be applied to identify time intervals where our model predictions are significantly lower or higher than the observations. In this regard, the innovation vector is used to pinpoint which mechanisms are absent in our model, where they operate, and which population of electrons they affect the most.

Mixed pitch angle-energy diffusion subtracts PSD from our model, and its effect is stronger at higher K (section 6.1), than at lower K (section 6.2). Similar results have been reported by others (Albert & Young, 2005; Albert et al., 2009; Subbotin et al., 2010; Xiao et al., 2010) relying on 2-D (pitch angle and energy diffusion) and 3-D simulations. The contribution of mixed pitch angle-energy diffusion at low K and high μ (last two cases in section 6.2) warrants a more detailed study in the future.

The scattering effect induced by EMIC waves on electrons with energies above $\sim$2 MeV and equatorial pitch angles less than $\sim$40° to 60° (both second and third cases in sections 6.1 and 6.2) is consistent with previous modeling and observational studies (Drozdov et al., 2017; Shprits, Subbotin, et al., 2013; Shprits et al., 2016; Xiang et al., 2017). Visual analysis of the corresponding average innovation plots, before and after including EMIC waves for $\mu = 300$ MeV G^{-1} and $K = 0.8$ G$^{0.5}$ R$_E$, and for $\mu = 600$ MeV G^{-1} and $K = 0.8$ G$^{0.5}$ R$_E$, show that, for a fixed K, the losses brought by introducing EMIC waves, are larger for higher μ than for lower μ. Similar effects are observed for $K = 0.1$ G$^{0.5}$ R$_E$. Specifically, such losses are mostly evident in the region with $2 < Kp < 4$ and $L^* < 5$, on average. Our findings provide supporting evidence that EMIC waves certainly provide an additional loss mechanism and play an essential role in the dynamics of the ultrarelativistic electron population.

Magnetopause shadowing driven by the LCDS effectively brings losses into our model, as concluded by earlier studies, which relied either on observations or simulations (Shprits et al., 2006; Turner et al., 2012; Yu et al., 2013; Turner, Angelopoulos, Morley, et al., 2014; Xiang et al., 2017). In our case, the average innovation plots show that this mechanism is more efficient in the intervals with $2 < Kp < 4$ and in the region with $L^* > 5$. For the two populations of electrons with the lowest μ values (both first cases in section 6.1 and 6.2), the incorporation of this process into the data assimilative scheme clearly illustrates a region of large underestimation extending from $L^* = 5.4$ up to the boundary at $L^* = 6.6$, corresponding to the absence of magnetospheric convection in our reanalysis. Such a process is accounted for by other models, such as the VERB-4D code (Aseev et al., 2016; Shprits et al., 2015), which solves the modified Fokker-Planck equation with additional convection terms.

Previous works have shed some light on the role and importance of mixed pitch angle-energy diffusion, scattering by EMIC waves, and magnetopause shadowing in the dynamics of the radiation belt electrons, and the current study is in agreement with their findings. Nevertheless, quantitative assessments of the contribution of each process have been scarce (Yu et al., 2013). The innovation vector certainly provides a tool to objectively determine how much loss is caused by each mechanism and to estimate the relative percentage of their contribution to the total dynamics. This analysis will be included in our future studies.

Lastly, we plan to perform a long-term reanalysis (several years spanning different levels of geomagnetic activity) and reconstruct the radial profiles of radiation belt electron PSD for the entire duration of current missions like the Van Allen Probes and Arase (Miyoshi et al., 2018). Data assimilation will play a crucial role in the analysis of such measurements and will be used to quantitatively report on the contribution of different mechanisms to the dynamical evolution of electron PSD. This will ultimately allow us to achieve a better understanding of the physical processes causing acceleration, transport, and losses in the radiation belts.

Appendix A: Adiabatic Invariants

The first adiabatic invariant is associated with the gyration of a particle around the field line and may be expressed as

$$\mu = \frac{p_\perp^2}{2m_0 B}, \tag{A1}$$

where $p_\perp$ is the relativistic momentum in the direction perpendicular to the direction of the magnetic field, m_0 is the electron rest mass, and B is the magnitude of the local magnetic field.

The second adiabatic invariant associated with the bounce motion between the mirror points may be expressed as

$$J = \int_{\text{bounce}} p_\parallel \, ds = 2\sqrt{2\mu m_0} \int_{S_m}^{S'_m} \sqrt{B_m - B(s)} \, ds, \tag{A2}$$

where $p_\parallel$ is the relativistic momentum in the direction parallel to the direction of the magnetic field, B_m is the magnetic field strength at the mirror point, S_m and S'_m are the distances along the field line from the equator to the mirror point, and ds is the distance element along the field line.

The K invariant is a combination of the first two invariants, and it does not depend on the charge or the mass of the particle. It is usually expressed as:

$$K = \frac{J}{2\sqrt{2m_0\mu}} = \int_{S_m}^{S'_m} \int \sqrt{B_m - B(s)} \, ds \tag{A3}$$

The third adiabatic invariant is associated with the drift motion around the Earth and may be expressed in terms of the magnetic flux through the orbit:

$$\Phi = \int_{\text{drift}} B \, ds. \tag{A4}$$

The Roederer parameter L^* (Roederer, 1970) is commonly used instead of Φ:

$$L^* = \frac{2\pi M}{\Phi R_{\text{E}}} \tag{A5}$$

where M is the Earth's magnetic moment.

In a dipolar magnetic field, the equatorial pitch angle of electrons α_0 can be related to the invariant K as (Schulz & Lanzerotti, 1974):

$$y\sqrt{\frac{L}{0.31}}K - 2.7604(1 - y) - 0.6396(y\ln y + 2y - 2\sqrt{y}) = 0 \tag{A6}$$

where $y = \sin(\alpha)$.

The kinetic energy of a particle can be related to the first adiabatic invariant as

$$E_k = E_0 \left\{ \sqrt{\left(\frac{2B\mu}{E_0 \sin^2(\alpha)} + 1 \right)} - 1 \right\} \tag{A7}$$

At any L shell PSD f may be related to the differential flux as (Rossi and Olbert, 1970):

$$f = \frac{10^3}{2.9979 \cdot 10^{10}} \frac{j}{p^2 c^2} \tag{A8}$$

where j is the differential flux in units of $(\text{sr s cm}^2 \text{ keV})^{-1}$, pc is in units of MeV, and PSD is in $(\text{MeV/c cm})^{-3}$.

References

Albert, J., Meredith, N., & Horne, R. (2009). Three-dimensional diffusion simulation of outer radiation belt electrons during the 9 October 1990 magnetic storm. *Journal of Geophysical Research*, *114*, A09214. https://doi.org/10.1029/2009JA014336

Albert, J., & Young, S. (2005). Multidimensional quasi-linear diffusion of radiation belt electrons. *Geophysical Research Letters*, *32*, L14110. https://doi.org/10.1029/2005GL023191

Aseev, N., Shprits, Y., Drozdov, A., & Kellerman, A. (2016). Numerical applications of the advective-diffusive codes for the inner magnetosphere. *Space Weather*, *14*, 993–1010. https://doi.org/10.1002/2016SW001484

Baker, D. (2002). How to cope with space weather. *Science*, *297*(5586), 1486–1487.

Baker, D., Allen, J., Kanekal, S., & Reeves, G. (1998). Disturbed space environment may have been related to pager satellite failure, Eos. *Transactions of the American Geophysical Union*, *79*(40), 477–483.

Baker, D., Erickson, P., Fennell, J., Foster, J., Jaynes, A., & Verronen, P. (2018). Space weather effects in the Earth's radiation belts. *Space Science Reviews*, *214*(1), 17.

Baker, D., Kanekal, S., Hoxie, V., Batiste, S., Bolton, M., Li, X., et al. (2012). The Relativistic Electron-Proton Telescope (REPT) instrument on board the Radiation Belt Storm Probes (RBSP) spacecraft: Characterization of Earth's radiation belt high-energy particle populations. In *The Van Allen Probes Mission* (pp. 337–381). Boston, MA: Springer.

Blake, J., Carranza, P., Claudepierre, S., Clemmons, J., Crain, W., Dotan, Y., et al. (2013). The Magnetic Electron Ion Spectrometer (MagEIS) instruments aboard the Radiation Belt Storm Probes (RBSP) spacecraft. In *The Van Allen Probes Mission* (pp. 383–421). Boston, MA: Springer.

Bourdarie, S., & Maget, V. (2012). Electron radiation belt data assimilation with an ensemble Kalman filter relying on the Salammbô code. *Annales Geophysicae*, *30*, 929–943. https://doi.org/10.5194/angeo-30-929-2012

Brautigam, D., & Albert, J. (2000). Radial diffusion analysis of outer radiation belt electrons during the October 9, 1990, magnetic storm. *Journal of Geophysical Research*, *105*(A1), 291–309.

Carpenter, D., & Anderson, R. (1992). An ISEE/whistler model of equatorial electron density in the magnetosphere. *Journal of Geophysical Research*, *97*(A2), 1097–1108.

Craven, J. (1966). Temporal variations of electron intensities at low altitudes in the outer radiation zone as observed with satellite Injun 3. *Journal of Geophysical Research*, *71*(23), 5643–5663.

Daae, M., Shprits, Y., Ni, B., Koller, J., Kondrashov, D., & Chen, Y. (2011). Reanalysis of radiation belt electron phase space density using various boundary conditions and loss models. *Advances in Space Research*, *48*(8), 1327–1334.

Drozdov, A., Shprits, Y., Orlova, K., Kellerman, A., Subbotin, D., Baker, D., et al. (2015). Energetic, relativistic, and ultrarelativistic electrons: Comparison of long-term VERB code simulations with Van Allen Probes measurements. *Journal of Geophysical Research: Space Physics*, *120*, 3574–3587. https://doi.org/10.1002/2014JA020637

Drozdov, A., Shprits, Y., Usanova, M., Aseev, N., Kellerman, A., & Zhu, H. (2017). EMIC wave parameterization in the long-term VERB code simulation. *Journal of Geophysical Research: Space Physics*, *122*, 8488–8501. https://doi.org/10.1002/2017JA024389

Evensen, G. (1994). Sequential data assimilation with a nonlinear quasi-geostrophic model using Monte Carlo methods to forecast error statistics. *Journal of Geophysical Research*, *99*(C5), 10,143–10,162.

Fennell, J., H. Koons, J. Roeder, and J. Blake (2001). Spacecraft charging: Observations and relationship to satellite anomalies, Tech. rep., Aerospace Corp.

Ghil, M., & Malanotte-Rizzoli, P. (1991). Data assimilation in meteorology and oceanography. In *Advances in geophysics* (Vol. 33, pp. 141–266). Elsevier.https://doi.org/10.1016/S0065-2687(08)60442-2

Green, J., Likar, J., & Shprits, Y. (2017). Impact of space weather on the satellite industry. *Space Weather*, *15*, 804–818. https://doi.org/10.1002/2017SW001646

Hanser, F. (2011). EPS/HEPAD calibration and data handbook (Tech. Rep. GOESN-ENG-048D). Carlisle, MA: Assurance Technology Corporation.

Horne, R., Meredith, N., Thorne, R., Heynderickx, D., Iles, R., & Anderson, R. (2003). Evolution of energetic electron pitch angle distributions during storm time electron acceleration to megaelectronvolt energies. *Journal of Geophysical Research: Space Physics*, *108*(A1), 1016. https://doi.org/10.1029/2001JA009165

Horne, R., & Thorne, R. (1998). Potential waves for relativistic electron scattering and stochastic acceleration during magnetic storms. *Geophysical Research Letters*, *25*(15), 3011–3014.

Jazwinski, A. (1970). Stochastic and filtering theory. Mathematics in Sciences and Engineering Series, Series 64.

Kalman, R. (1960). A new approach to linear filtering and prediction problems. *Journal of Basic Engineering*, *82*(1), 35–45.

Kalnay, E. (2003). *Atmospheric modeling, data assimilation and predictability*. New York: Cambridge University Press.

Kellerman, A., Shprits, Y., Kondrashov, D., Subbotin, D., Makarevich, R., Donovan, E., & Nagai, T. (2014). Three-dimensional data assimilation and reanalysis of radiation belt electrons: Observations of a four-zone structure using five spacecraft and the VERB code. *Journal of Geophysical Research: Space Physics*, *119*, 8764–8783. https://doi.org/10.1002/2014JA020171

Koller, J., Chen, Y., Reeves, G., Friedel, R., Cayton, T., & Vrugt, J. (2007). Identifying the radiation belt source region by data assimilation. *Journal of Geophysical Research*, *112*, A06244. https://doi.org/10.1029/2006JA012196

Kondrashov, D., Shprits, Y., Ghil, M., & Thorne, R. (2007). A Kalman filter technique to estimate relativistic electron lifetimes in the outer radiation belt. *Journal of Geophysical Research*, *112*, A10227. https://doi.org/10.1029/2007JA012583

Lahoz, W., Khattatov, B., & Ménard, R. (2010). Data assimilation and information. In *Data Assimilation*, (pp. 3–12). Berlin, Heidelberg: Springer.

Lohmeyer, W., Carlton, A., Wong, F., Bodeau, M., Kennedy, A., & Cahoy, K. (2015). Response of geostationary communications satellite solid-state power amplifiers to high-energy electron fluence. *Space Weather*, *13*, 298–315. https://doi.org/10.1002/2014SW001147

Mauk, B., Fox, N. J., Kanekal, S., Kessel, R., Sibeck, D., & Ukhorskiy, A. (2012). Science objectives and rationale for the Radiation Belt Storm Probes mission. In *The Van Allen Probes Mission* (pp. 3–27). Boston, MA: Springer.

Mazur, J., Fennell, J., Roeder, J., O'Brien, P., Guild, T., & Likar, J. (2011). The timescale of surface-charging events. *IEEE Transactions on Plasma Science*, *40*(2), 237–245.

Meredith, N., Horne, R., Kersten, T., Fraser, B., & Grew, R. (2014). Global morphology and spectral properties of EMIC waves derived from CRRES observations. *Journal of Geophysical Research: Space Physics*, *119*, 5328–5342. https://doi.org/10.1002/2014JA020064

Meredith, N., Thorne, R., Horne, R., Summers, D., Fraser, B., & Anderson, R. (2003). Statistical analysis of relativistic electron energies for cyclotron resonance with EMIC waves observed on CRRES. *Journal of Geophysical Research*, *108*(A6), 1250. https://doi.org/10.1029/2002JA009700

Miyoshi, Y., Shinohara, I., Takashima, T., Asamura, K., Higashio, N., Mitani, T., et al. (2018). Geospace exploration project ERG. *Earth, Planets and Space*, *70*(1), 101.

Naehr, S., & Toffoletto, F. (2005). Radiation belt data assimilation with an extended Kalman filter. *Space Weather*, *3*(6), 1–15.

Ni, B., Shprits, Y., Friedel, R., Thorne, R., Daae, M., & Chen, Y. (2013). Responses of Earth's radiation belts to solar wind dynamic pressure variations in 2002 analyzed using multisatellite data and Kalman filtering. *Journal of Geophysical Research: Space Physics*, *118*, 4400–4414. https://doi.org/10.1002/jgra.50437

Ni, B., Shprits, Y., Nagai, T., Thorne, R., Chen, Y., Kondrashov, D., & Kim, H. (2009). Reanalyses of the radiation belt electron phase space density using nearly equatorial CRRES and polar-orbiting Akebono satellite observations. *Journal of Geophysical Research*, *114*, A05208. https://doi.org/10.1029/2008JA013933

Ni, B., Shprits, Y., Thorne, R., Friedel, R., & Nagai, T. (2009). Reanalysis of relativistic radiation belt electron phase space density using multisatellite observations: Sensitivity to empirical magnetic field models. *Journal of Geophysical Research: Space Physics*, *114*, A12208. https://doi.org/10.1029/2009JA014438

Onsager, T. G., Grubb, R., Kunches, J., Matheson, L., Speich, D., Zwickl, R., & Sauer, H. (1996). Operational uses of the GOES energetic particle detectors. InE. R. Washwell (Eds.), *GOES-8 and Beyond: 7–9 August 1996, Denver, Colorado, Proc. SPIE Int. Soc. Opt. Eng.,* (Vol. 2812, pp. 281). Bellingham, WA: International Society for Optics and Photonics.

Orlova, K., & Shprits, Y. (2014). Model of lifetimes of the outer radiation belt electrons in a realistic magnetic field using realistic chorus wave parameters. *Journal of Geophysical Research: Space Physics*, *119*, 770–780. https://doi.org/10.1002/2013JA019596

Orlova, K., Spasojevic, M., & Shprits, Y. (2014). Activity-dependent global model of electron loss inside the plasmasphere. *Geophysical Research Letters*, *41*, 3744–3751. https://doi.org/10.1002/2014GL060100

Roederer, J. (1970). *Dynamics of geomagnetically trapped radiation*. New York: Springer-Verlag.

Rossi, B.,Olbert, S. (1970). *Introduction to the physics of space*. New York: McGraw-Hill.

Rothwell, P., & McIlwain, C. (1960). Magnetic storms and the Van Allen radiation belts: Observations from satellite 1958ε (Explorer IV). *Journal of Geophysical Research*, *65*(3), 799–806.

Schulz, M., & Lanzerotti, L. (1974). *Particle Diffusion in the Radiation Belts*. New York: Springer.

Shprits, Y., Daae, M., & Ni, B. (2012). Statistical analysis of phase space density buildups and dropouts. *Journal of Geophysical Research*, *117*, A01219. https://doi.org/10.1029/2011JA016939

Shprits, Y., Drozdov, A., Spasojevic, M., Kellerman, A., Usanova, M., Engebretson, M., et al. (2016). Wave-induced loss of ultra-relativistic electrons in the Van Allen radiation belts. *Nature Communications*, *7*, 12,883.

Shprits, Y., Kellerman, A., Aseev, N., Drozdov, A., & Michaelis, I. (2017). Multi-MeV electron loss in the heart of the radiation belts. *Geophysical Research Letters*, *44*, 1204–1209. https://doi.org/10.1002/2016GL072258

Shprits, Y., Kellerman, A., Drozdov, A., Spence, H., Reeves, G., & Baker, D. (2015). Combined convective and diffusive simulations: VERB-4D comparison with 17 March 2013 Van Allen Probes observations. *Geophysical Research Letters*, *42*, 9600–9608. https://doi.org/10.1002/2015GL065230

Shprits, Y., Kellerman, A., Kondrashov, D., & Subbotin, D. (2013). Application of a new data operator-splitting data assimilation technique to the 3-D VERB diffusion code and CRRES measurements. *Geophysical Research Letters*, *40*, 4998–5002. https://doi.org/10.1002/grl.50969

Shprits, Y., Kondrashov, D., Chen, Y., Thorne, R., Ghil, M., Friedel, R., & Reeves, G. (2007). Reanalysis of relativistic radiation belt electron fluxes using CRRES satellite data, a radial diffusion model, and a Kalman filter. *Journal of Geophysical Research*, *112*, A11214. https://doi.org/10.1029/2006JA011657

Shprits, Y., & Ni, B. (2009). Dependence of the quasi-linear scattering rates on the wave normal distribution of chorus waves. *Journal of Geophysical Research*, *114*, A11205. https://doi.org/10.1029/2009JA014223

Shprits, Y., Subbotin, D., Drozdov, A., Usanova, M., Kellerman, A., Orlova, K., et al. (2013). Unusual stable trapping of the ultrarelativistic electrons in the Van Allen radiation belts. *Nature Physics*, *9*(11), 699.

Shprits, Y., Subbotin, D., Meredith, N., & Elkington, S. (2008). Review of modeling of losses and sources of relativistic electrons in the outer radiation belt II: Local acceleration and loss. *Journal of Atmospheric and Solar-Terrestrial Physics*, *70*(14), 1694–1713.

Shprits, Y., Subbotin, D., & Ni, B. (2009). Evolution of electron fluxes in the outer radiation belt computed with the VERB code. *Journal of Geophysical Research: Space Physics*, *114*, A11209. https://doi.org/10.1029/2008JA013784

Shprits, Y., Thorne, R., Friedel, R., Reeves, G., Fennell, J., Baker, D., & Kanekal, S. (2006). Outward radial diffusion driven by losses at magnetopause. *Journal of Geophysical Research*, *111*, A11214. https://doi.org/10.1029/2006JA011657

Singer, H. J., Matheson, L., Grubb, R., Newman, A., & Bouwer, S. D. (1996). Monitoring space weather with the GOES magnetometers. In E. R. Washwell (Ed.), *SPIE Conference Proceedings, GOES-8 and Beyond* (Vol. 2812, pp. 299–308). Bellingham, WA: SPIE Int. Soc. Opt. Eng.

Sorenson, H. (1985). *Kalman filtering: Theory and application*. Los Alamitos: IEEE Press.

Spence, H., Reeves, G., Baker, D., Blake, J., Bolton, M., Bourdarie, S., et al. (2013). Science goals and overview of the Radiation Belt Storm Probes (RBSP) Energetic particle, Composition, and Thermal plasma (ECT) suite on NASA's Van Allen Probes mission. *Space Science Reviews*, *179*(1-4), 311–336.

Stratton, J., Harvey, R., & Heyler, G. (2012). Mission overview for the Radiation Belt Storm Probes mission. In *The Van Allen Probes Mission* (pp. 29–57). Boston, MA: Springer.

Subbotin, D., & Shprits, Y. (2009). Three-dimensional modeling of the radiation belts using the Versatile Electron Radiation Belt (VERB) code. *Space Weather*, *7*, S10001. https://doi.org/10.1029/2008SW000452

Subbotin, D., Shprits, Y., & Ni, B. (2010). Three-dimensional VERB radiation belt simulations including mixed diffusion. *Journal of Geophysical Research*, *115*, A03205. https://doi.org/10.1029/2009JA015070

Talagrand, O. (1997). Assimilation of observations, an introduction. *Journal of the Meteorological Society of Japan. Ser. II*, *75*(1B), 191–209.

Tsyganenko, N., & Sitnov, M. (2007). Magnetospheric configurations from a high-resolution data-based magnetic field model. *Journal of Geophysical Research*, *112*, A06225. https://doi.org/10.1029/2007JA012260

Turner, D., Angelopoulos, V., Li, W., Bortnik, J., Ni, B., Ma, Q., et al. (2014). Competing source and loss mechanisms due to wave-particle interactions in Earth's outer radiation belt during the 30 September to 3 October 2012 geomagnetic storm. *Journal of Geophysical Research: Space Physics*, *119*, 1960–1979. https://doi.org/10.1002/2014JA019770

Turner, D., Angelopoulos, V., Morley, S., Henderson, M., Reeves, G., Li, W., et al. (2014). On the cause and extent of outer radiation belt losses during the 30 September 2012 dropout event. *Journal of Geophysical Research: Space Physics*, *119*, 1530–1540. https://doi.org/10.1002/2013JA019446

Turner, D., Shprits, Y., Hartinger, M., & Angelopoulos, V. (2012). Explaining sudden losses of outer radiation belt electrons during geomagnetic storms. *Nature Physics*, *8*(3), 208.

Usanova, M., Drozdov, A., Orlova, K., Mann, I., Shprits, Y., Robertson, M., et al. (2014). Effect of EMIC waves on relativistic and ultrarelativistic electron populations: Ground-based and Van Allen Probes observations. *Geophysical Research Letters*, *41*, 1375–1381. https://doi.org/10.1002/2013GL059024

Walt, M. (2005). *Introduction to geomagnetically trapped radiation*. New York: Cambridge University Press.

Xiang, Z., Tu, W., Li, X., Ni, B., Morley, S., & Baker, D. (2017). Understanding the mechanisms of radiation belt dropouts observed by Van Allen Probes. *Journal of Geophysical Research: Space Physics*, *122*, 9858–9879. https://doi.org/10.1002/2017JA024487

Xiao, F., Su, Z., Zheng, H., & Wang, S. (2010). Three-dimensional simulations of outer radiation belt electron dynamics including cross-diffusion terms. *Journal of Geophysical Research*, *115*, A05216. https://doi.org/10.1029/2009JA014541

Yu, Y., Koller, J., & Morley, S. K. (2013). Quantifying the effect of magnetopause shadowing on electron radiation belt dropouts. *Annales Geophysicae*, *31*, 1929–1939. https://doi.org/10.5194/angeo-31-1929-2013